

Pathryoshka: Compressing Pathology Foundation Models via Multi-Teacher Knowledge Distillation with Nested Embeddings

Christian Grashei^{*1,3,4} Christian Brechenmacher^{*2} Rao Muhammad Umer² Jingsong Liu^{1,4}
 Carsten Marr² Ewa Szczerka^{†,2} Peter J. Schüffler^{†,1,3,4}

¹Technical University of Munich, ²Helmholtz Munich, ³Munich Data Science Institute, ⁴Munich Center for Machine Learning

Abstract

Pathology foundation models (FMs) have driven significant progress in computational pathology. However, these high-performing models can easily exceed a billion parameters and produce high-dimensional embeddings, thus limiting their applicability for research or clinical use when computing resources are tight.

Here, we introduce Pathryoshka, a multi-teacher distillation framework inspired by RADIO distillation and Matryoshka Representation Learning to reduce pathology FM sizes while allowing for adaptable embedding dimensions. We evaluate our framework with a distilled model on ten public pathology benchmarks with varying downstream tasks. Compared to its much larger teachers, Pathryoshka reduces the model size by 86-92% at on-par performance. It outperforms state-of-the-art single-teacher distillation models of comparable size by a median margin of 7.0 in accuracy. By enabling efficient local deployment without sacrificing accuracy or representational richness, Pathryoshka democratizes access to state-of-the-art pathology FMs for the broader research and clinical community.

1. Introduction

Empirical scaling laws demonstrate consistent performance gains from increasing foundation model size, with larger models capturing more complex structures and showing stronger performance across tasks [17, 22, 41]. Yet, model scaling brings also rapid cost escalation, yielding state-of-the-art development and deployment inaccessible. This challenge is acute in pathology: although pathology foundation models (FMs) promise major advances in cancer diagnosis and patient care [5, 32], their hardware and operational costs hinder adoption in resource-limited clinics and research centers. Pathology FMs contain hundreds of millions to billions of parameters, and with whole-slide images requiring

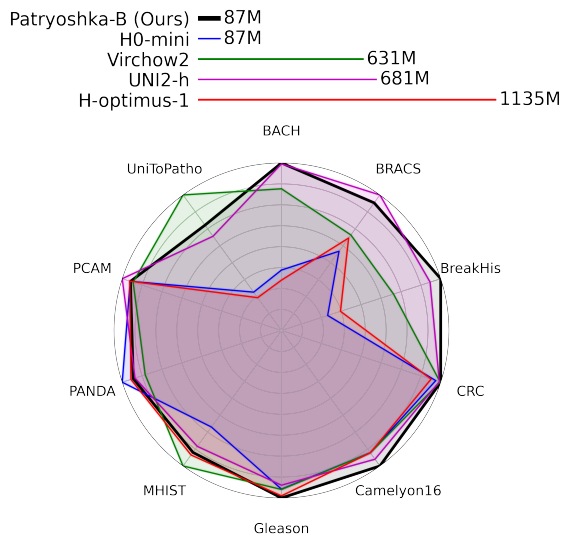


Figure 1. Although smaller in parameter size (see legend), our model outperforms or is on par with state of the art pathology foundation models on various benchmarks. If models of one family possess insufficiencies in one area (here H-optimus-1 in breast cancer histopathology image analysis), a single-teacher distillation model of the same family (H0-mini) possesses the same insufficiencies.

thousands of tiles to be encoded inference and storage costs become prohibitive. Thus, there is a clear need for pathology FMs with compressed model and embedding sizes that maintain performance while enabling compute- and memory-efficient deployment.

While several promising approaches exist in this direction, they still face notable limitations. Naively training smaller models on equally rich datasets does not match the performance of larger models [25]. A prominent approach to reducing model size while preserving accuracy is *knowledge distillation*, which transfers knowledge from large teacher models to a smaller student by aligning their embeddings or logits [18, 19, 30, 36]. Although highly effective compared to naive approaches such as model ensembling, and

^{*}Equal contribution.

[†]Equal supervision.

able to substantially reduce model size [11, 31], distillation typically retains large embedding sizes, leading to high inference times and memory usage in downstream tasks. To obtain compact embeddings, *Matryoshka Representation Learning* [26, 40] draws inspiration from matryoshka dolls, training a single high-dimensional embedding whose prefix sub-vectors remain semantically meaningful and effective. This nested structure enables truncation to lower dimensions with minimal loss. However, while Matryoshka learning compresses embeddings, it does not guarantee overall model size reduction. To our knowledge, no prior work has combined distillation with Matryoshka learning to jointly realize the benefits of both approaches.

In the context of pathology FMs, distillation is typically performed using a single teacher model, such as H0-mini [16] trained by distillation from a large vision transformer model called H-optimus-0 [37]. However, relying on a single teacher risks inheriting its biases and limits the represented diversity of clinical variation. We illustrate this behavior in Fig. 1, where the distilled H0-mini is only able to perform as good or only marginally better than H-optimus-1 [6], a model trained as successor to H-optimus-0. While multi-teacher distillation strategies such as AM-RADIO [36] have been successfully applied to general image foundation models, they have not yet been explored in pathology. **In summary, pathology FMs still lack a method that simultaneously compresses both model and embedding size while leveraging diverse multi-teacher signals while accounting for data heterogeneity.**

To address these challenges, we propose Pathryoshka, a pathology FM that leverages multi-teacher knowledge distillation in combination with Matryoshka representation learning to fundamentally reduce model size and improve computational efficiency while achieving similar performances to large teacher models [6, 11, 28, 45] and outperforming previous distilled small models [16] as illustrated in Fig. 1. The hierarchical embedding structure of Pathryoshka fuses complementary signals from multiple teachers into compact and robust subembeddings. To avoid memorization of embeddings of teacher models from public training data while ensuring enough data diversity, distillation training of Pathryoshka is performed on an internal dataset of 243 million image tiles extracted from 158,233 H&E-stained images across all organs, which is augmented using a novel cropping strategy. Evaluations on multiple benchmarks, including patch-level (e.g., PCAM, Gleason), slide-level (e.g., Camelyon16, CRC), and image retrieval (CCRCC), demonstrate that Pathryoshka consistently outperforms individual teacher models in terms of efficiency and performance. Our main contributions are the following:

- We introduce a **multi-teacher distillation framework** for unsupervised distillation of pathology FMs that relies solely on the CLS and patch tokens, enabling the use of

external public models.

- We propose **nested embeddings** for multi-teacher distillation, yielding a pathology foundation model with adaptable embeddings.
- We demonstrate that multiple large-scale pathology FM teacher models can be effectively compressed into a **single compact model with competitive performance**, substantially reducing model size and inference cost.
- We introduce a novel **cropping-based augmentation strategy** tailored specifically for multi-teacher distillation in digital pathology, improving representation alignment across teachers.

2. Related Work

Current Pathology Foundation Models Recent years witnessed a surge of pathology FMs leveraging vision transformer architecture [13] and self-supervised learning on large, diverse unlabeled datasets to learn generalizable representations that can be efficiently adapted to many downstream pathology tasks with minimal labeled data [12, 14, 15, 29, 37, 42, 43, 45]. Among most prominent pathology FMs, three large models have shown excellent performance: Virchow2, UNI2-h, and H-optimus-1. Virchow2 [45] is a 632-million-parameter vision transformer model (ViT-H/14) for pathology, extending the earlier Virchow model [42] and pretrained on an unprecedented dataset of 3.1 million H&E-stained whole-slide images (WSIs) from 225,000 patients, totaling 2 billion image tiles. A larger variant, Virchow2G (1.9-billion parameters, ViT-G), was also introduced to examine pure model scaling effects. UNI2-h [12] is a 681-million-parameter model (ViT-H/14) pretrained on over 200 million tiles from more than 350,000 H&E WSIs across 20 major tissue types. H-optimus-1 [6] is a 1.1-billion-parameter ViT-G/14 model pretrained on over one million H&E WSIs, comprising billions of tiles. Despite these advances, adoption of current resource-hungry pathology FMs in the clinic remains limited, and no single model provides both optimal efficiency and performance across all pathology tasks.

Distillation for Pathology Foundation Models So far, only *single*-teacher distillation has been studied for reducing pathology FMs size. One example is H0-mini [16], a model distilled from H-optimus-0 (ViT-G) into a smaller (ViT-B) architecture with 87M parameters. Another model is Virchow2G-Mini (ViT-S), using 22M parameters, distilled from Virchow2G (ViT-G). We are not aware of any pathology FM that would be trained by distillation from multiple significantly larger teachers. Moreover, none of the pathology FM distillation frameworks used nested embeddings for downstream tasks.

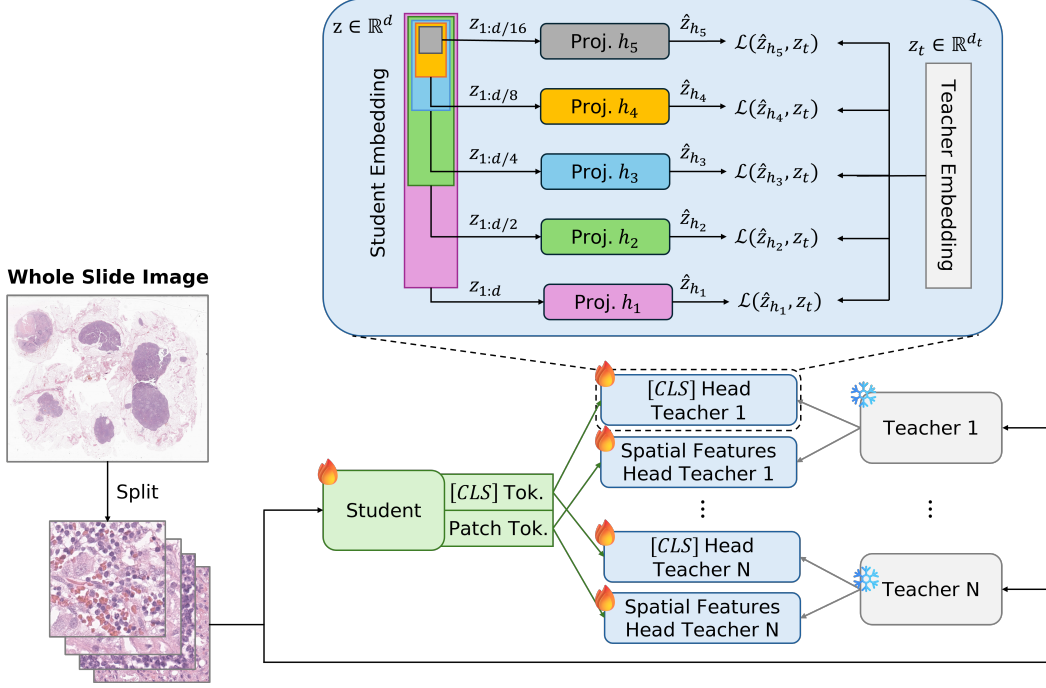


Figure 2. Overview of the proposed Pathryoshka, a multi-teacher distillation framework. The student model and distillation heads are jointly trained while teacher models remain frozen. Input images are augmented and processed by both the student and all teachers. The CLS and spatial feature heads align student representations with those of the teachers. Each head includes multiple MLP projection layers that form nested embeddings by minimizing a similarity loss between student and teacher projections.

3. Method

We introduce Pathryoshka, a framework for distilling multiple foundation models into a single, compact vision transformer (Fig. 2). The framework features nested embeddings to increase computational efficiency in downstream tasks. Our framework draws inspiration from AM-RADIO [36], an approach for agglomerative distillation using multiple teachers, as well as from Matryoshka Representation Learning [26] for flexible embeddings of varying dimensionalities.

While demonstrated for histopathology, our proposed setup is domain-agnostic, enabling application in other fields where multiple homogeneous models are available. It operates in a fully unsupervised manner, requiring only a large-scale unlabeled dataset.

3.1. Dataset

To train our model, we used a large-scale in-house dataset of 158,233 H&E stained whole-slide images (WSIs). Tissue regions were identified using CLAM [27]. A maximum of 2,250 tiles of size 448x448 pixels were randomly sampled per WSI at 10x, 20x and 40x magnifications in proportions of 20%, 40% and 40%, respectively, to cover multiple morphological scales. If there was not enough tissue on a WSI, sampling was stopped earlier, resulting in a total of 243 million tiles.

We intentionally exclude public datasets from training to ensure a fair and unbiased evaluation. In the context of distillation, separating training and evaluation data is particularly important to avoid the student model to memorize teacher embeddings for seen data, and to be able to demonstrate generalization to unseen inputs.

3.2. Data Augmentation

Since the dataset originates from a single institution and was digitized using a single scanner, we apply extensive augmentations to enhance its diversity, including color augmentation, random flipping and Gaussian blur. For color augmentation, we employ H&E-specific stain perturbations from the Albumentations library [10], that decomposes an image into the hematoxylin and eosin channels before perturbing their intensities to simulate more realistic stain variations. Additionally, we incorporate a novel cropping-based augmentation dedicated to our multi-teacher framework as explained in Sec. 3.4.

3.3. Multi-Teacher Distillation Framework

Our framework consists of a ViT student model and multiple teacher models. The student aims to learn the representations provided by the teachers by a novel cropping strategy, multi-teacher nested embeddings, adjusted distillation heads and

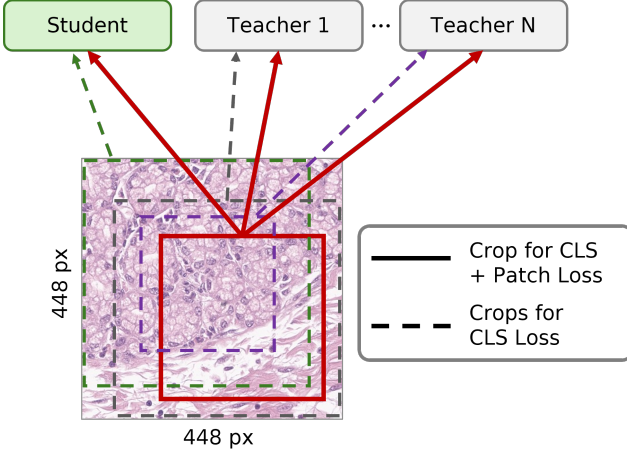


Figure 3. A random crop is obtained from the input image. This aligned crop is individually color augmented for the student and all teachers. We compute the CLS and patch loss for this aligned crop to make sure that the patch tokens are aligned for all models. Additionally, each model receives a second random individual crop which aims to improve magnification invariance. We only compute CLS loss on this non-aligned crop.

specific loss formulations, as explained in the following sections.

3.4. Cropping Strategy

We generate multiple crops per tile to train the model (Fig. 3). Each crop covers between 25% and 100% of the tile area with an aspect ratio sampled from $[0.9, 1.1]$, followed by random horizontal and vertical flips. The resulting region is resized to 224×224 px. Formally, let x denote an image tile from the dataset, a_{spatial} the random cropping and flipping augmentation, and a_{visual} a random H&E stain and blur augmentation. The *aligned crop* x_c is defined as:

$$x_c = a_{\text{spatial}}(x) \quad (1)$$

The student model and all teacher models receive a color augmented version of that aligned crop. Additionally, the student model and all teacher models receive a individual random crop called *non-aligned crop* that is color augmented as well. Those crops cover different areas of the original tile, effectively simulating variations in magnification and thereby improving robustness. Formally, let $\mathcal{M} = f_s, f_{t_1}, \dots, f_{t_N}$ denote the set of student and teachers. Each model $f_m \in \mathcal{M}$ produces two outputs:

$$z_m^a = f_m(a_{\text{visual}}(x_c)), z_m^g = f_m(a_{\text{visual}}(a_{\text{spatial}}(x))). \quad (2)$$

Here, z_m^a is the output for the aligned crop and z_m^g the output for the non-aligned crop. Each output z_m comprises the CLS token and patch embeddings of the respective model. For the aligned crop we compute a loss for both

the CLS token and the patch tokens. For the non-aligned crop, we only compute a loss for the CLS token that doesn't require strict spatial correspondence.

Note, that *DINOv2 distillation* [33] would require to forward the CLS token and patch tokens through the DINO and iBOT head, respectively, to obtain the high-dimensional teacher *prototype scores*. However, the weights for the DINO and iBOT head are often not publicly available making DINOv2 distillation practically impossible. In contrast, our method does not require any heads for the teachers and attaches distillation heads only to the student allowing different embedding dimensions for student and teachers.

3.5. Nested Embeddings

We incorporate nested embeddings [26], which allow the distilled model to generate representations that adapt to varying computational budgets and downstream requirements.

Given an input x , the distilled model produces an embedding $z \in \mathbb{R}^d$. We aim to learn embeddings where any prefix $z_{1:m}$, with $m \leq d$, forms semantically meaningful representation. Let M denote the set of target embedding sizes. For each $m \in M$, we enforce representational consistency through a loss-based constraint. Following [40], we adopt a geometrically decreasing series of nested embedding sizes $M = \{768, 384, 192, 96, 48\}$, obtained by halving the dimension for each level. At training time, we compute distillation losses at all nesting levels, ensuring that truncated representations $z_{1:m}$ remain semantically aligned with teacher features.

3.6. Distillation Heads

We employ three-layer MLPs to project the outputs of the distilled student to the embedding dimension of the respective teacher. The size of the first MLP layer matches the student embedding and the last layer the embedding size of the teacher model. We set the intermediate layer to the same dimensionality as the teacher embeddings to avoid creating an additional bottleneck. This design ensures that the only compression in the network occurs between the teacher and student embedding spaces.

Two sets of projection heads are used per teacher. One set is for the CLS token and the other set for the patch tokens, that encode spatial information. Each set of projection heads consists of multiple MLPs equal to the number of nesting levels $|M|$. Each MLP is responsible for one nesting level of dimension m and receives the first m features of the embedding.

3.7. Loss Formulation

The training targets of our student model are the outputs of multiple teacher models. Since all teachers are vision transformers, each produces a global CLS token, which

captures image-level information, and a set of patch tokens that encode spatial features.

Let x denote the augmented input image. The student network, parameterized by Θ , outputs a sequence of tokens:

$$\mathbf{z} = f(x|\Theta) = [z_s, z_p^{(1)}, z_p^{(2)}, \dots, z_p^{(N)}], \quad (3)$$

where $z_s \in \mathbb{R}^d$ is the global CLS token and $z_p^{(i)} \in \mathbb{R}^d$ are the N patch tokens, each representing a spatial region of the input.

Similarly, the output for teacher t with parameters Θ_t is denoted as

$$\mathbf{z}^t = f_t(x|\Theta_t) = [z_s^{(t)}, z_p^{(t,1)}, z_p^{(t,2)}, \dots, z_p^{(t,N)}], \quad (4)$$

where $z_s^{(t)}, z_p^{(t,i)} \in \mathbb{R}^{d_t}$.

For every teacher t , we attach two families of distillation heads:

$$g_s^{(t,m)} : \mathbb{R}^m \rightarrow \mathbb{R}^{d_t}, \quad g_p^{(t,m)} : \mathbb{R}^m \rightarrow \mathbb{R}^{d_t},$$

where $m \in M$ denotes the nesting dimension (i.e., the subset of the first m features) and M is the set of considered nesting levels. Each $g_s^{(t,m)}$ projects the first m dimensions of the student's CLS token to the teacher's embedding space, while $g_p^{(t,m)}$ performs an analogous projection for each patch token.

The projected features are defined as:

$$\hat{z}_s^{(t,m)} = g_s^{(t,m)}(z_{s,1:m}), \quad (5)$$

$$\hat{z}_p^{(t,i,m)} = g_p^{(t,m)}(z_{p,1:m}^{(i)}), \quad (6)$$

where $z_{s,1:m}$ and $z_{p,1:m}^{(i)}$ denote the first m dimensions of the corresponding embeddings.

The loss for the CLS token is computed as:

$$\mathcal{L}_{\text{cls}} = \sum_t \sum_m \mathcal{L}_{\text{cos}}(\hat{z}_s^{(t,m)}, z_s^{(t)}), \quad (7)$$

where \mathcal{L}_{cos} is the cosine similarity loss and $z_s^{(t)}$ denotes the teacher's CLS token.

Before computing the patch-level loss, we standardize each teacher's patch embeddings to account for differences in embedding magnitude, following [35]:

$$\hat{z}_p^{(t,i)} = \frac{z_p^{(t,i)} - \mu_c^t}{\sigma_c^t}, \quad (8)$$

where μ_c^t and σ_c^t are the mean and standard deviation computed over channel c of teacher t for the current batch.

Finally, the patch-level distillation loss is defined as:

$$\mathcal{L}_{\text{patch}} = \sum_t \sum_i \sum_m \mathcal{L}_{\text{MSE}}(\hat{z}_p^{(t,i,m)}, \hat{z}_p^{(t,i)}), \quad (9)$$

where \mathcal{L}_{MSE} denotes the mean squared error loss.

4. Implementation

We implement our framework with a ViT-B/14 (**Pathryoshka-B**) and ViT-S/14 (**Pathryoshka-S**) with register tokens as the student model. Training is performed on 8 GPUs with a total batch size of 1024 (including both aligned crops and non-aligned crops) using the AdamW optimizer. The learning rate follows a cosine annealing schedule from $1 \cdot 10^{-4}$ to $1 \cdot 10^{-5}$, and the weight decay is annealed from 0.01 to 0.02. The model is trained for 300k iterations.

We observe that the training losses for both the CLS token and the patch tokens remain relatively noisy throughout optimization. To stabilize training, we maintain an exponential moving average (EMA) of the student parameters, with a cosine-annealed decay rate that increases from 0.994 to 1.0 over the course of training. All evaluations are performed using the EMA model.

Unlike the AM-RADIO framework, our approach discards the teacher-matching heads after training, eliminating their contribution to inference cost. This ensures that the deployed model maintains the same computational efficiency as the standard vision transformer models.

4.1. Teacher Selection

Today, a plethora of pathology foundation models exist. We selected the three high-performing and well-known models Virchow2 [45], UNI2-h [11] and H-optimus-1 [6] as teacher models. All of them are large models (over 600M parameters) and high-ranked in current benchmarks. Note, that our method is agnostic to the number and size of the teacher models, and more teachers can easily be added. However, as the number of forward passes for every teacher and the student has to be the same, the required training resources scale with the inference cost of the teacher models.

5. Experiments and Results

We evaluate Pathryoshka in two sizes: Pathryoshka-B (87M parameters) and Pathryoshka-S (22M), and compare them to their teacher models and to the state-of-the-art single-teacher distilled pathology FM, H0-mini. Because H0-mini matches Pathryoshka-B in size and uses the same ViT-B/14 backbone, it serves as the default baseline. Across multiple public patch-level and slide-level benchmarks, Pathryoshka-B achieves performance competitive with its much larger teachers and surpasses H0-mini, while Pathryoshka-S retains considerably high performance despite being four times smaller than Pathryoshka-B. Furthermore, we evaluate how the different nesting levels behave also compared against FMs without such an ordering in their embeddings.

Dataset	Teacher				Ours	
	Virchow2	UNI2-h	H-optimus-1	H0-mini	Pathryoshka-S	Pathryoshka-B
BACH	88.00 (0.46)	<u>90.69</u> (1.13)	78.07 (0.76)	79.19 (0.46)	85.75 (0.47)	90.80 (0.30)
BRACS	62.24 (0.73)	66.08 (0.87)	61.94 (0.49)	60.61 (0.59)	61.70 (1.02)	<u>65.33</u> (0.22)
BreakHis	81.88 (0.59)	<u>85.94</u> (0.33)	76.05 (1.20)	74.70 (0.93)	76.23 (0.41)	87.06 (0.71)
CRC	<u>96.61</u> (0.15)	96.51 (0.19)	95.53 (0.04)	96.07 (0.19)	95.99 (0.04)	96.67 (0.12)
Gleason	77.94 (0.58)	77.45 (0.27)	78.46 (0.49)	77.87 (0.51)	<u>78.69</u> (0.84)	78.70 (0.58)
MHIST	86.27 (0.09)	82.57 (0.32)	83.74 (0.29)	79.03 (0.24)	82.20 (0.39)	<u>84.03</u> (0.19)
Patch Cam.	93.80 (0.12)	95.12 (0.05)	<u>94.22</u> (0.12)	94.15 (0.1)	92.07 (0.06)	94.12 (0.06)
CAM. 16	93.09 (1.35)	<u>93.76</u> (1.26)	92.06 (1.25)	93.09 (1.71)	93.54 (1.28)	94.98 (1.03)
PANDA	75.78 (1.01)	76.77 (1.06)	<u>77.22</u> (1.38)	78.05 (0.37)	76.20 (0.93)	76.97 (0.78)
UniToPatho	57.45 (0.25)	53.95 (0.27)	48.74 (0.61)	49.21 (0.34)	52.65 (0.42)	<u>54.90</u> (0.10)
Median	84.08	<u>84.26</u>	78.26	78.54	80.45	85.55

Table 1. Results for the public benchmark datasets for our model in comparison to the baseline H0-mini and the teacher models Virchow2, UNI2-h and H-optimus-1. We report the average multiclass accuracy for multi-class classification and binary balanced accuracy for binary classification tasks over five runs as reported by the *eva* evaluation framework. Highlighted are **best** and second best models.

Model	Params. [M] (↓)	FLOPs [G] (↓)	Throughput [img/s] (↑)
Virchow2	631	329.11	134.3 ± 7.9
UNI2-h	681	360.71	134.6 ± 7.6
H-optimus-1	1,135	591.81	82.5 ± 4.3
Pathryoshka-S	22	11.05	2483.7 ± 28.4
Pathryoshka-B	87	44.60	885.1 ± 7.1
H0-mini	87	44.60	885.1 ± 7.1

Table 2. Computational efficiency statistics, including parameter count, FLOPs, and inference time per image (measured on an RTX 3090 GPU).

5.1. Classification Benchmark Results

We evaluate all models on ten commonly used public pathology benchmarks. Eight of those are patch-level tasks (BACH [1], BRACS [7], BreakHis [38], CRC 100k [23], Gleason Grading [2], MHIST [44], Patch Camelyon [39], and UniToPatho [3]), and two are slide-level tasks (CAMELYON16 [4] and PANDA [9]). The selected benchmarks cover a wide range of magnifications levels from 0.25 microns per pixel (mpp) to 3.5 mpp. For all public benchmarks we used the *eva* [21] benchmark framework. This framework uses a single linear layer for patch classification tasks and an ABMIL [20] head for slide-level classification tasks to classify the CLS embedding of the respective model. To ensure a fair comparison of our models with the baseline and the teachers, we run the benchmarks for all models using *eva*’s default configuration. We report the average of five

runs of the multiclass classification accuracy for multiclass tasks and binary balanced accuracy for binary classification tasks. The results are shown in Table 1.

Compared to its much larger teacher models, Pathryoshka-B delivers competitive performance across the tested benchmark datasets. It exceeds the median accuracy of UNI2-h by 1.29 points, Virchow2 by 1.47 points, and H-optimus-1 by 7.29 points, despite requiring 86%, 87%, and 92% fewer parameters, respectively. Furthermore, it surpasses its baseline, H0-mini, by 7.01 points in median accuracy, while additionally providing nested embeddings. With a four-fold reduction in parameters compared to Pathryoshka-B, Pathryoshka-S shows a 5.1-point drop in median accuracy; however, its performance still exceeds that of both H0-mini and H-optimus-1.

An ablation study of the random-cropping strategy introduced in Section 3 demonstrates its effectiveness: incorporating random cropping improves the average accuracy of Pathryoshka-B by 0.74 points and median by 0.22 across the public benchmarks. Detailed results appear in the Appendix Tab. 7.

Table 2 compares parameter counts and inference efficiency of the evaluated models, reporting FLOPs and throughput (images per second) measured on a consumer-grade RTX 3090 GPU. Throughput is computed in FP16 precision with a batch size of 32, and we report the mean and standard deviation over 500 batches. Our best-performing model, Pathryoshka-B, uses 92% fewer parameters and achieves roughly 11× higher throughput compared to its largest teacher, H-optimus-1. In whole slide image analysis, where thousands of image patches must be encoded for a

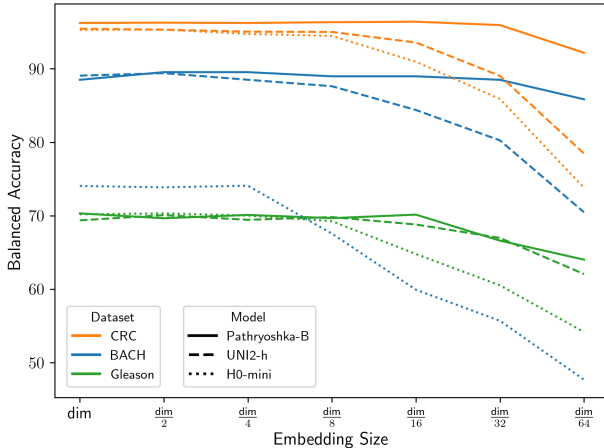


Figure 4. **Comparison of k-NN classification** accuracy between Pathryoshka-B, the best-performing teacher model UNI2-h, and the baseline H0-mini, across three multiclass classification benchmarks. Each point corresponds to a subembedding of decreasing dimensionality (e.g., “ $\frac{\text{dim}}{2}$ ” denotes using only half of the full embedding size). Colors indicate different datasets. Line types denote the respective models. As a result of the nested embedding structure, our model maintains high accuracy even when using smaller subembeddings. Note that UNI2-h uses 1536-dimensional embeddings, while our model and H0-mini use 768-dimensional embeddings.

single prediction, this efficiency translates into substantial reductions in total processing time.

5.2. Benefits from Nested Embeddings

k-NN-Classification In Fig. 4, we evaluate the quality of the learned representations by performing k-NN-based classification on three multiclass patch classification benchmarks. Cosine similarity is used as the distance metric with $k = 10$. Pathryoshka-B is compared against the best-performing teacher model UNI2-h and the baseline H0-mini. Note that the embedding dimension of UNI2-h is twice that of both Pathryoshka-B and H0-mini.

Due to the nested embedding design, the features of our model are inherently ordered by relevance. To assess this property, we perform k-NN classification using only the first $\frac{\text{dim}}{n}$ features of our model for $n \in [1, 2, 4, 8, 16, 32, 64]$. For the other models, we match the dimensionality by randomly sampling $\frac{\text{dim}}{n}$ indices of their embeddings and selecting the corresponding features. Each random sampling is repeated five times, and we report results for our model along with the mean and standard deviation across runs for the other models (see Table 3).

Interestingly, the performance remains relatively stable for all models up to $\frac{\text{dim}}{8}$, suggesting a degree of redundancy in the embeddings of UNI2-h and H0-mini. Beyond this point, both UNI2-h and H0-mini show a accuracy drop on the CRC and BACH datasets. H0-mini also shows a significant

drop for the Gleason dataset. In contrast, Pathryoshka-B maintains stable performance up to $\frac{\text{dim}}{32}$ and only mildly decreasing for $\frac{\text{dim}}{64}$, despite being trained only up to a nested size of $\frac{\text{dim}}{16}$.

This behavior is further supported by the embedding visualizations in Figure 5. Despite truncation, Pathryoshka-B preserves semantic structure that is lost in UNI2-h, the strongest teacher model. For this comparison, embeddings were taken from the same arbitrary image, and truncation was applied identically by retaining the initial segment of each embedding. As truncation increases, Pathryoshka-B embeddings continue to reflect the original patch structure, whereas UNI2-h embeddings become progressively blurred and eventually lose all recognizable patterns.

Patch Retrieval We further evaluate the quality of nested embeddings via a patch retrieval task. For each query patch, the top- k nearest patches are retrieved based on cosine similarity, and accuracy is measured by label agreement with the query. The experiment is conducted on the CCRCC dataset [8] using frozen backbones for all models. As shown in Table 4, Pathryoshka-B matches the retrieval performance of large-scale teacher models while surpassing all baselines at a compressed embedding size of $\frac{\text{dim}}{32}$ and $\frac{\text{dim}}{64}$, demonstrating that its nested embeddings remain compact yet semantically consistent.

6. Discussion and Conclusion

In this work, we introduced Pathryoshka, a pathology FM that integrates multi-teacher distillation with nested embeddings. This approach departs from the conventional paradigm that associates performance gains with scaling model size or dataset volume. Instead, Pathryoshka achieves lightweight architecture and fast inference while maintaining performance comparable to large state-of-the-art pathology FMs and outperforming small ones.

Our results show that multi-teacher distillation surpasses conventional single-teacher approaches in pathology tasks. While single-teacher distillation inherits the biases and blind spots of a single supervision source, the multi-teacher strategy integrates complementary knowledge from multiple experts, producing more robust and generalizable student models. We also demonstrate the practical gains from training nested embeddings. With decreasing Pathryoshka embedding size, performance in classification and retrieval tasks decreases only slightly, while offering significant computational efficiency gains.

While effective, our approach still has several limitations. First, all WSIs in our dataset come from a single institution and scanner, limiting data diversity and potentially affecting out-of-distribution performance. Despite this limited variability, fusing knowledge from multiple experts via multi-

Dataset	Model	dim	$\frac{\text{dim}}{2}$	$\frac{\text{dim}}{4}$	$\frac{\text{dim}}{8}$	$\frac{\text{dim}}{16}$	$\frac{\text{dim}}{32}$	$\frac{\text{dim}}{64}$
BACH	UNI2-h	89.06	89.40 (1.01)	88.50 (0.85)	87.62 (1.79)	84.38 (3.91)	80.25 (3.46)	70.47 (1.22)
	H0-mini	74.05	73.87 (1.17)	74.08 (2.54)	67.56 (2.45)	59.93 (4.53)	55.70 (4.69)	47.68 (2.23)
	Pathryoshka-B	88.50	89.54	89.54	88.97	88.97	88.50	85.85
CRC	UNI2-h	95.45	95.32 (0.18)	95.05 (0.19)	95.01 (0.44)	93.57 (1.04)	89.03 (0.95)	78.47 (4.49)
	H0-mini	95.28	95.33 (0.45)	94.73 (0.20)	94.47 (0.51)	90.95 (0.58)	85.88 (2.73)	73.80 (3.61)
	Pathryoshka-B	96.24	96.27	96.23	96.34	96.40	95.94	92.17
Gleason	UNI2-h	69.37	70.08 (0.96)	69.44 (0.95)	69.82 (1.96)	68.80 (1.52)	66.98 (2.61)	62.06 (1.37)
	H0-mini	70.20	70.32 (1.79)	70.02 (2.96)	69.26 (2.77)	64.79 (4.98)	60.52 (3.73)	54.18 (2.43)
	Pathryoshka-B	70.32	69.65	70.11	69.67	70.15	66.61	64.02

Table 3. KNN classification accuracy with reduced embedding dimensions. For our distilled model, we use the nested embeddings. Since UNI2-h and H0-mini do not provide an ordering of the features within the embedding, we randomly sample indices corresponding to each target embedding size and report the mean accuracy over five runs, with standard deviation shown in parentheses.

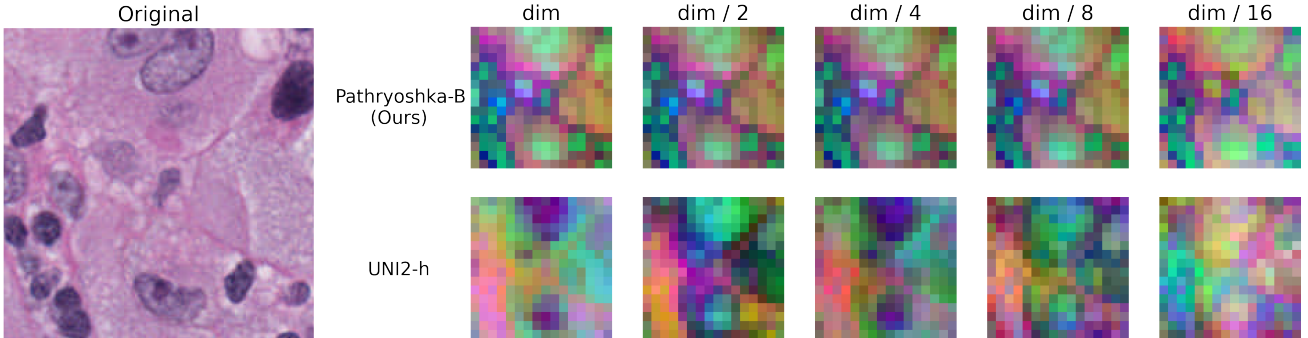


Figure 5. Example patch embedding visualization. While both models create an interpretable embedding representation, our model is able to retain the semantical representation throughout the truncation process. The different cells are still distinguishable in higher compression. The colors in the visualization correspond to the first three principal components obtained through PCA applied to the high-dimensional embeddings. Each RGB channel represents a principal axis capturing the most significant variance in the embedding space.

Model	dim	$\frac{\text{dim}}{2}$	$\frac{\text{dim}}{4}$	$\frac{\text{dim}}{8}$	$\frac{\text{dim}}{16}$	$\frac{\text{dim}}{32}$	$\frac{\text{dim}}{64}$
Virchow2	<u>97.2</u>	<u>97.2</u>	<u>97.1</u>	97.1	97.0	96.6	<u>94.8</u>
UNI2-h	<u>97.2</u>	97.1	97.0	<u>97.0</u>	96.7	95.6	92.4
H-optimus-1	<u>97.1</u>	97.1	97.0	<u>97.0</u>	96.6	<u>95.7</u>	92.7
Pathryoshka-B	97.1	97.1	97.0	<u>97.0</u>	<u>96.9</u>	96.6	95.2
H0-mini	97.4	97.3	97.2	<u>97.0</u>	96.6	95.5	92.6

Table 4. Patch-retrieval experiment results on the CCRCC dataset. We report the average Recall@5 over all queries. Results for $K = 1$ and $K = 10$ are provided in the Appendix Tab. 5. Pathryoshka-B exhibits minimal degradation when the feature dimensionality is reduced, indicating efficient information compression and strong representation compactness compared to teacher and baseline models.

teacher distillation, combined with extensive data augmentation and our cropping strategy, enabling competitive performance. Second, while multi-teacher distillation improves robustness over single-teacher approaches, residual biases may remain when teachers share correlated blind spots, high-

lighting the importance of careful teacher selection. The benefit of diverse, high-quality teachers in maximizing complementary strengths, versus the reduced gains from overly similar or poorly curated teachers, remain to be fully quantified. Finally, our evaluation focuses on well-established classification and representation benchmarks that capture many practical needs in pathology, but it does not exhaustively cover all clinically relevant tasks, leaving room for future work.

Despite these limitations, our experiments show that Pathryoshka effectively compresses both model and embedding sizes compared to previous large pathology FMs while maintaining strong benchmark performance, even with a significant reduction in representational dimensionality. In doing so, Pathryoshka can be deployed on substantially smaller architectures, opening the avenue to adoption of pathology FMs in low-resource clinics and research institutions.

References

[1] Guilherme Aresta, Teresa Araújo, Scotty Kwok, Sai Saketh Chennamsetty, Mohammed Safwan, Varghese Alex, Bahram Marami, Marcel Prastawa, Monica Chan, Michael Donovan, et al. Bach: Grand challenge on breast cancer histology images. *Medical image analysis*, 56:122–139, 2019. 6

[2] Eirini Arvaniti, Kim S Fricker, Michael Moret, Niels Rupp, Thomas Hermanns, Christian Fankhauser, Norbert Wey, Peter J Wild, Jan H Rueschoff, and Manfred Claassen. Automated gleason grading of prostate cancer tissue microarrays via deep learning. *Scientific reports*, 8(1):12054, 2018. 6

[3] Carlo Alberto Barbano, Daniele Perlo, Enzo Tartaglione, Attilio Fiandrotti, Luca Bertero, Paola Cassoni, and Marco Grangetto. Unitopatho, a labeled histopathological dataset for colorectal polyps classification and adenoma dysplasia grading. In *2021 IEEE International Conference on Image Processing (ICIP)*, pages 76–80. IEEE, 2021. 6

[4] Babak Ehteshami Bejnordi, Mitko Veta, Paul Johannes Van Diest, Bram Van Ginneken, Nico Karssemeijer, Geert Litjens, Jeroen AWM Van Der Laak, Meyke HermSEN, Quirine F Manson, Maschenka Balkenhol, et al. Diagnostic assessment of deep learning algorithms for detection of lymph node metastases in women with breast cancer. *Jama*, 318(22):2199–2210, 2017. 6

[5] Mohsin Bilal, Aadam, Manahil Raza, Youssef Altherwy, Anas Alsuhaiabi, Abdulrahman Abduljabbar, Fahdah Almarshad, Paul Golding, and Nasir Rajpoot. Foundation models in computational pathology: A review of challenges, opportunities, and impact, 2025. 1

[6] Bioptimus. H-optimus-1, 2025. 2, 5

[7] Nadia Brancati, Anna Maria Anniciello, Pushpak Pati, Daniel Riccio, Giosuè Scognamiglio, Guillaume Jaume, Giuseppe De Pietro, Maurizio Di Bonito, Antonio Foncubierta, Gerardo Botti, et al. Bracs: A dataset for breast carcinoma subtyping in h&e histology images. *Database*, 2022:baac093, 2022. 6

[8] Otso Brummer, Petri Pöllönen, Satu Mustjoki, and Oscar Brück. Computational textural mapping harmonises sampling variation and reveals multidimensional histopathological fingerprints. *British Journal of Cancer*, 129(4):683–695, 2023. 7

[9] Wouter Bulten, Kimmo Kartasalo, Po-Hsuan Cameron Chen, Peter Ström, Hans Pinckaers, Kunal Nagpal, Yuannan Cai, David F Steiner, Hester Van Boven, Robert Vink, et al. Artificial intelligence for diagnosis and gleason grading of prostate cancer: the panda challenge. *Nature medicine*, 28(1):154–163, 2022. 6

[10] Alexander Buslaev, Vladimir I. Iglovikov, Eugene Khvedchenya, Alex Parinov, Mikhail Druzhinin, and Alexandr A. Kalinin. Albumentations: Fast and flexible image augmentations. *Information*, 11(2), 2020. 3

[11] Richard J Chen, Tong Ding, Ming Y Lu, Drew FK Williamson, Guillaume Jaume, Bowen Chen, Andrew Zhang, Daniel Shao, Andrew H Song, Muhammad Shaban, et al. Towards a general-purpose foundation model for computational pathology. *Nature Medicine*, 2024. 2, 5

[12] Richard J Chen, Tong Ding, Ming Y Lu, Drew FK Williamson, Guillaume Jaume, Andrew H Song, Bowen Chen, Andrew Zhang, Daniel Shao, Muhammad Shaban, et al. Towards a general-purpose foundation model for computational pathology. *Nature medicine*, 30(3):850–862, 2024. 2

[13] Alexey Dosovitskiy. An image is worth 16x16 words: Transformers for image recognition at scale. *arXiv preprint arXiv:2010.11929*, 2020. 2

[14] Alexandre Filiot, Ridouane Ghermi, Antoine Olivier, Paul Jacob, Lucas Fidon, Alice Mac Kain, Charlie Saillard, and Jean-Baptiste Schiratti. Scaling Self-Supervised Learning for Histopathology with Masked Image Modeling, 2023. 2

[15] Alexandre Filiot, Paul Jacob, Alice Mac Kain, and Charlie Saillard. Phikon-v2, A large and public feature extractor for biomarker prediction, 2024. 2

[16] Alexandre Filiot, Nicolas Dop, Oussama Tchita, Auriane Riou, Rémy Dubois, Thomas Peeters, Daria Valter, Marin Scalbert, Charlie Saillard, Geneviève Robin, and Antoine Olivier. Distilling foundation models for robust and efficient models in digital pathology. In *Medical Image Computing and Computer Assisted Intervention – MICCAI 2025*, pages 162–172, Cham, 2026. Springer Nature Switzerland. 2

[17] Tatsunori Hashimoto. Model performance scaling with multiple data sources. In *Proceedings of the 38th International Conference on Machine Learning*, pages 4107–4116. PMLR, 2021. 1

[18] Greg Heinrich, Mike Ranzinger, Hongxu Yin, Yao Lu, Jan Kautz, Andrew Tao, Bryan Catanzaro, and Pavlo Molchanov. Radiov2. 5: Improved baselines for agglomerative vision foundation models. In *Proceedings of the Computer Vision and Pattern Recognition Conference*, pages 22487–22497, 2025. 1

[19] Geoffrey Hinton, Oriol Vinyals, and Jeff Dean. Distilling the knowledge in a neural network. *arXiv [stat.ML]*, 2015. 1

[20] Maximilian Ilse, Jakub Tomczak, and Max Welling. Attention-based deep multiple instance learning. In *International conference on machine learning*, pages 2127–2136. PMLR, 2018. 6

[21] kaiko.ai, Ioannis Gatopoulos, Nicolas Käning, Roman Moser, and Sebastian Otálora. eva: Evaluation framework for pathology foundation models. In *Medical Imaging with Deep Learning*, 2024. 6

[22] Jared Kaplan, Sam McCandlish, Tom Henighan, Tom B. Brown, Benjamin Chess, Rewon Child, Scott Gray, Alec Radford, Jeffrey Wu, and Dario Amodei. Scaling laws for neural language models, 2020. 1

[23] Jakob Nikolas Kather, Niels Halama, and Alexander Marx. 100,000 histological images of human colorectal cancer and healthy tissue (v0.1). <https://doi.org/10.5281/zenodo.1214456>, 2018. Zenodo, Dataset. 6

[24] Jakob Nikolas Kather, Niels Halama, and Alexander Marx. 100,000 histological images of human colorectal cancer and healthy tissue, 2018. 1

[25] Masakata Kawai, Noriaki Ota, and Shinsuke Yamaoka. Large-scale pretraining on pathological images for fine-tuning of small pathological benchmarks. In *Medical Image Learning with Limited and Noisy Data*, pages 257–267, Cham, 2023. Springer Nature Switzerland. 1

[26] Aditya Kusupati, Gantavya Bhatt, Aniket Rege, Matthew Wallingford, Aditya Sinha, Vivek Ramanujan, William

Howard-Snyder, Kaifeng Chen, Sham Kakade, Prateek Jain, et al. Matryoshka representation learning. *Advances in Neural Information Processing Systems*, 35:30233–30249, 2022. 2, 3, 4

[27] Ming Y Lu, Drew FK Williamson, Tiffany Y Chen, Richard J Chen, Matteo Barbieri, and Faisal Mahmood. Data-efficient and weakly supervised computational pathology on whole-slide images. *Nature biomedical engineering*, 5(6):555–570, 2021. 3

[28] Ming Y Lu, Bowen Chen, Drew F K Williamson, Richard J Chen, Ivy Liang, Tong Ding, Guillaume Jaume, Igor Odintsov, Long Phi Le, Georg Gerber, Anil V Parwani, Andrew Zhang, and Faisal Mahmood. A visual-language foundation model for computational pathology. *Nature Medicine*, 30(3):863–874, 2024. 2

[29] Ming Y. Lu, Bowen Chen, Drew F. K. Williamson, Richard J. Chen, Ivy Liang, Tong Ding, Guillaume Jaume, Igor Odintsov, Long Phi Le, Georg Gerber, Anil V. Parwani, Andrew Zhang, and Faisal Mahmood. A visual-language foundation model for computational pathology. *Nature Medicine*, 30(3):863–874, 2024. 2

[30] Jiabo Ma, Zhengrui Guo, Fengtao Zhou, Yihui Wang, Yingxue Xu, Jinbang Li, Fang Yan, Yu Cai, Zhengjie Zhu, Cheng Jin, et al. A generalizable pathology foundation model using a unified knowledge distillation pretraining framework. *Nature Biomedical Engineering*, pages 1–20, 2025. 1

[31] Peter Neidlinger, Omar S M El Nahhas, Hannah Sophie Muti, Tim Lenz, Michael Hoffmeister, Hermann Brenner, Marko van Treeck, Rupert Langer, Bastian Dislich, Hans Michael Behrens, Christoph Röcken, Sebastian Foersch, Daniel Truhn, Antonio Marra, Oliver Lester Saldanha, and Jakob Nikolas Kather. Benchmarking foundation models as feature extractors for weakly-supervised computational pathology. *arXiv [eess.IV]*, 2024. 2

[32] Mieko Ochi, Daisuke Komura, and Shumpei Ishikawa. Pathology foundation models, 2024. 1

[33] Maxime Oquab, Timothée Darcet, Théo Moutakanni, Huy Vo, Marc Szafraniec, Vasil Khalidov, Pierre Fernandez, Daniel Haziza, Francisco Massa, Alaaeldin El-Nouby, et al. Dinov2: Learning robust visual features without supervision. *arXiv preprint arXiv:2304.07193*, 2023. 4

[34] F. Pedregosa, G. Varoquaux, A. Gramfort, V. Michel, B. Thirion, O. Grisel, M. Blondel, P. Prettenhofer, R. Weiss, V. Dubourg, J. Vanderplas, A. Passos, D. Cournapeau, M. Brucher, M. Perrot, and E. Duchesnay. Scikit-learn: Machine learning in Python. *Journal of Machine Learning Research*, 12:2825–2830, 2011. 1

[35] Mike Ranzinger, Jon Barker, Greg Heinrich, Pavlo Molchanov, Bryan Catanzaro, and Andrew Tao. Phi-s: Distribution balancing for label-free multi-teacher distillation. *arXiv preprint arXiv:2410.01680*, 2024. 5

[36] Mike Ranzinger, Greg Heinrich, Jan Kautz, and Pavlo Molchanov. Am-radio: Agglomerative vision foundation model reduce all domains into one. In *Proceedings of the IEEE/CVF conference on computer vision and pattern recognition*, pages 12490–12500, 2024. 1, 2, 3

[37] Charlie Saillard, Rodolphe Jenatton, Felipe Llinares-López, Zelda Mariet, David Cahané, Eric Durand, and Jean-Philippe Vert. H-optimus-0, 2024. 2

[38] Fabio A Spanhol, Luiz S Oliveira, Caroline Petitjean, and Laurent Heutte. A dataset for breast cancer histopathological image classification. *Ieee transactions on biomedical engineering*, 63(7):1455–1462, 2015. 6

[39] Bastiaan S Veeling, Jasper Linmans, Jim Winkens, Taco Cohen, and Max Welling. Rotation equivariant cnns for digital pathology. In *International Conference on Medical image computing and computer-assisted intervention*, pages 210–218. Springer, 2018. 6

[40] Shashanka Venkataraman, Valentinos Pariza, Mohammadreza Salehi, Lukas Knobel, Spyros Gidaris, Elias Ramzi, Andrei Bursuc, and Yuki M Asano. Franca: Nested matryoshka clustering for scalable visual representation learning. *arXiv preprint arXiv:2507.14137*, 2025. 2, 4

[41] Pablo Villalobos, Jaime Sevilla, Tamay Besiroglu, Lennart Heim, Anson Ho, and Marius Hobbahn. Machine learning model sizes and the parameter gap, 2022. 1

[42] Eugene Vorontsov, Alican Bozkurt, Adam Casson, George Shaikovski, Michal Zelechowski, Kristen Severson, Eric Zimmermann, James Hall, Neil Tenenholz, Nicolo Fusi, et al. A foundation model for clinical-grade computational pathology and rare cancers detection. *Nature medicine*, 30(10):2924–2935, 2024. 2

[43] Xiyue Wang, Sen Yang, Jun Zhang, Minghui Wang, Jing Zhang, Wei Yang, Junzhou Huang, and Xiao Han. Transformer-based unsupervised contrastive learning for histopathological image classification. *Medical Image Analysis*, 81:102559, 2022. 2

[44] Jerry Wei, Arief Suriawinata, Bing Ren, Xiaoying Liu, Mikhail Lisovsky, Louis Vaickus, Charles Brown, Michael Baker, Naofumi Tomita, Lorenzo Torresani, et al. A petri dish for histopathology image analysis. In *International Conference on Artificial Intelligence in Medicine*, pages 11–24. Springer, 2021. 6

[45] Eric Zimmermann, Eugene Vorontsov, Julian Viret, Adam Casson, Michal Zelechowski, George Shaikovski, Neil Tenenholz, James Hall, Thomas Fuchs, Nicolo Fusi, Siqi Liu, and Kristen Severson. Virchow2: Scaling self-supervised mixed magnification models in pathology. *arXiv preprint arXiv:2408.00738*, 2024. 2, 5

Pathryoshka: Compressing Pathology Foundation Models via Multi-Teacher Knowledge Distillation with Nested Embeddings

Supplementary Material

7. Additional experiments results

Patch retrieval We report the complete patch-retrieval results for $K = 1$ and $K = 10$ on the CCRCC dataset in Table 5. These results complement the main-text analysis by showing consistent behavior across different recall values and compression levels.

Recall@1 (CCRCC)						
Model	dim	dim/2	dim/4	dim/8	dim/16	dim/32
Virchow2	97.7	97.7	97.7	97.7	97.5	97.2
UNI2-h	97.6	97.5	97.6	97.4	97.3	96.3
H-Optimus-1	97.7	97.8	97.7	97.5	97.2	96.5
Pathryoshka-B	97.6	97.6	97.6	97.6	97.4	97.3
H0-mini	98.0	97.9	97.9	97.7	97.1	96.3
Recall@10 (CCRCC)						
Model	dim	dim/2	dim/4	dim/8	dim/16	dim/32
Virchow2	96.8	96.8	96.8	96.7	96.5	96.0
UNI2-h	96.8	96.7	96.7	96.6	96.3	95.1
H-Optimus-1	96.7	96.7	96.6	96.5	96.1	95.2
Pathryoshka-B	96.7	96.7	96.6	96.5	96.5	94.7
H0-mini	97.0	96.9	96.7	96.5	96.1	94.8

Table 5. Complete patch-retrieval results for $K = 1$ and $K = 10$ on the CCRCC dataset. Pathryoshka-B demonstrates consistently stable performance across compression levels and recall metrics.

Time efficiency when using nested embeddings The k-nearest-neighbor (k-NN) classifier is deterministic with respect to the input data and algorithmic parameters, with the theoretical runtime complexity of k-NN classification being $\mathcal{O}(nd)$, where n denotes the number of samples and d the dimensionality of the embeddings. Consequently, the observed computation time is primarily dependent on the input size and embedding dimensionality. Smaller embedding sizes can therefore significantly speed up computation. We conducted an experiment on the runtime behavior of k-NN classification on the CRC 100k dataset [24] with different embedding sizes using the k-NN implementation of scikit-learn [34]. The mean runtimes for different embedding sizes across five runs are shown in Table 6. Our measurements confirm that computation time increases approximately linearly with the embedding dimension.

Per-teacher influence on embedding alignment Table 8 shows the impact analysis of the different teachers on the

dim	dim/2	dim/4	dim/16	dim/32	dim/64
13.55s	6.64s	3.15s	1.46s	0.62s	0.19s

Table 6. Mean computation efficiency increases on the scikit-learn implementation of the KNN classification task when using nested embeddings. Times were taken on the CRC100k dataset. When using a bigger dataset, the computation time scales approximately linearly.

Dataset	Pathryoshka-B crop	Pathryoshka-B no crop
BACH	90.80 (0.30)	90.04 (0.45)
BRACS	65.33 (0.22)	64.64 (0.72)
BreakHis	87.06 (0.71)	85.54 (0.56)
CRC	96.67 (0.12)	95.96 (0.09)
Gleason	78.70 (0.58)	77.73 (0.32)
MHIST	84.03 (0.19)	85.12 (0.23)
Patch Cam.	94.12 (0.06)	93.64 (0.04)
CAM. 16	94.98 (1.03)	91.62 (1.52)
PANDA	76.97 (0.78)	76.97 (1.18)
UniToPatho	54.90 (0.10)	54.89 (0.19)
Average	82.36	81.62
Median	85.55	85.33

Table 7. Ablation study of our random cropping strategy. We train Pathryoshka-B with (crop) and without (no crop) the proposed strategy introduced in Sec. 3.4. Random cropping improves performance on 8 out of the 10 public classification benchmarks. On average, it increases accuracy by 0.74 percentage points, and by 0.22 percentage points in terms of the median.

embedding creation using cosine similarity distance. UNI2-h, together with H-optimus-1, show the strongest alignment with the student in the summary embedding space, indicating that the student most closely reproduces their high-level summary representations. By contrast, in the feature embedding space the student is substantially closer to Virchow2 and H-optimus-1 than to UNI2-h, which implies that low-level feature representations in the student are dominated by Virchow2 and H-optimus-1 (visualized in figure 6). The relatively low standard deviation for UNI2-h in the summary space suggests a more consistent input, whereas the large standard deviation for Virchow2 in the feature space indicates that its influence on the student is more input-dependent. H-optimus-1 shows a similar mean impact to Virchow2 but with more stable alignment. Taken together,

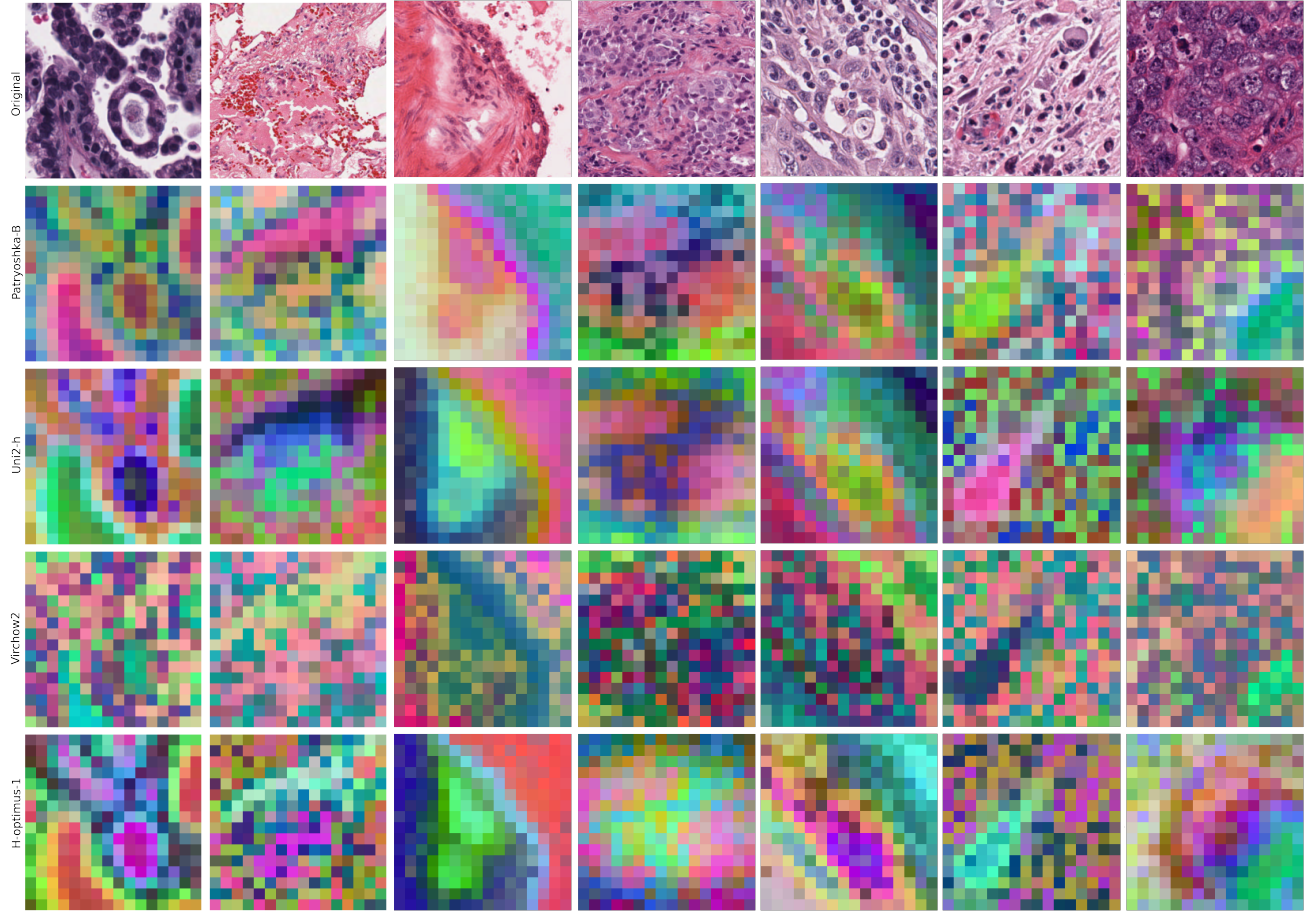


Figure 6. Pathryoshka represents features of the original image well, an important property for embedding-based similarity tasks, e.g. image retrieval. The PCA visualization of the models’ features reveals the individual teacher’s contribution to the distilled model. The three-component PCA maps their spatial embeddings to RGB pixel values.

	UNI2-h	Virchow2	H-optimus-1
Summary	0.544 (0.135)	0.616 (0.115)	0.566 (0.170)
Features	0.716 (0.146)	0.565 (0.295)	0.567 (0.210)

Table 8. Covariance distance between uncompressed summary and feature embeddings of the student heads to their respective teachers. UNI2-h possesses the highest conformance to our student model in the summary space, while in the feature space, Virchow2 and H-Optimus have higher impact.

these results suggest the student learned a hybrid representation: It adopts UNI2-h’s summary-level structure while drawing feature-level details primarily from Virchow2 and H-Optimus-1.

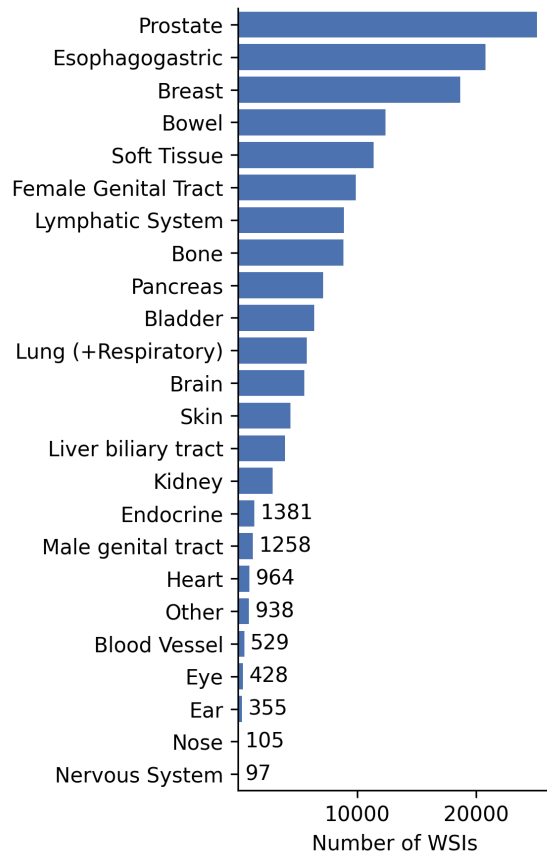


Figure 7. Organ distribution of whole slide images in the training set. Organ labels are provided only at the case level. Therefore, slide counts are approximate. For cases containing slides from multiple organs, the slides are evenly allocated across all associated organ labels.